Imaging of the strain field around precipitate particles using transmission ion channeling

King, P. J. C.; Breese, M. B. H.; Meekeson, D.; Smulders, P. J. M.; Wilshaw, P. R.; Grime, G. W.

Published in:
Journal of Applied Physics

DOI:
10.1063/1.363184

Imaging of the strain field around precipitate particles using transmission ion channeling

P. J. C. King, M. B. H. Breese, D. Meekeson, P. J. M. Smulders, P. R. Wilshaw, and G. W. Grime

Citation: Journal of Applied Physics **80**, 2671 (1996); doi: 10.1063/1.363184
View online: https://doi.org/10.1063/1.363184
View Table of Contents: http://aip.scitation.org/toc/jap/80/5
Published by the American Institute of Physics

Imaging of the strain field around precipitate particles using transmission ion channeling

P. J. C. King[a] and M. B. H. Breese
SPM Unit, Nuclear Physics Laboratory, University of Oxford, Keble Road, Oxford OX1 3RH, United Kingdom[b]

D. Meekeson
Department of Materials, University of Oxford, Parks Road, Oxford OX1 3PH, United Kingdom

P. J. M. Smulders
Nuclear Solid State Physics, Materials Science Centre, Groningen University, Nijenborgh 4, 9747 AG Groningen, The Netherlands

P. R. Wilshaw
Department of Materials, University of Oxford, Parks Road, Oxford OX1 3PH, United Kingdom

G. W. Grime
SPM Unit, Nuclear Physics Laboratory, University of Oxford, Keble Road, Oxford OX1 3RH, United Kingdom

(Received 10 April 1996; accepted for publication 24 May 1996)

This paper shows ion channeling images of the strain field produced by precipitate particles in a crystal matrix. Images have been produced by mapping the energy of 3 MeV protons transmitted through a thinned silicon crystal containing colonies of copper silicide particles, with the incident beam at or close to planar channeling directions of the lattice. Features of the precipitate contrast observed as a function of beam tilt angle away from channeling alignment are qualitatively explained using a model based on symmetrical plane rotation of the crystal lattice around the colonies. © *1996 American Institute of Physics.* [S0021-8979(96)05217-6]

I. INTRODUCTION

The established technique of ion channeling analysis[1] can be extended to give spatially resolved information when a scanned, focused ion beam from a nuclear microprobe is used. The method, called channeling scanning transmission ion microscopy (CSTIM), exploits the reduced energy loss rate of channeled ions to produce images of crystal defects such as dislocations and stacking faults. The presence of a defect locally disturbs the channeling process, causing either dechanneling or, in some instances, an enhancement of channeling. This in turn alters the mean energy loss of ions transmitted through the crystal that have passed through the defect region, when the incident beam is aligned with or close to a channeling direction. Images of a crystal based on the mean transmitted ion energy loss therefore reveal crystal imperfections.

CSTIM images of single and bunched misfit dislocations in $Si_{1-x}Ge_x$/Si crystals have been produced using this method.[2,3] Contrast changes exhibited by the dislocations in CSTIM images when the beam was tilted about the channeling direction were explained by considering the lattice plane rotation produced by the largest dislocation component in the top layer of the crystal. Subsequent computer simulation of the passage of channeled ions through a crystal with rotated lattice planes near its surface supported this explanation and revealed new features of the analysis.[4] CSTIM images showing elastic relaxation of $Si_{1-x}Ge_x$ layers grown on raised Si mesas have also been generated and quantitatively interpreted.[5] Stacking faults near the surface of a silicon crystal have also been imaged with the CSTIM technique, and it was demonstrated how the direction of stacking fault translation vectors can be determined.[6] It was also found that with the incident beam aligned just beyond one critical angle away from the channeling direction, the net effect of the faults was to cause channeling rather than to produce dechanneling.[7] This was interpreted as being due to a transition of some of the proton trajectories from blocked to channeling owing to the lattice translation at the fault plane.

Very little analysis of precipitate particles by traditional ion channeling using an unfocused beam has been undertaken, probably due to the complex nature of the dechanneling behavior that precipitates may be expected to produce.[1] Ion channeling results obtained using an unfocused beam cannot be readily interpreted since the lack of spatial resolution means that the different effects on channeling that a precipitate may produce are obscured. In this paper, we extend spatially resolved channeling analysis to include precipitate particles. In Sec. IV we show measured CSTIM images of a precipitate feature at different tilt angles to several planar channeling directions. Transmission electron microscopy examination of the specimen is then described in Sec. V. The observed changes in transmitted proton energy with beam angle to the channeling planes are then explained in Sec. VI using a model based on symmetrical lattice plane rotation around the precipitate particles. In Sec. VII, good agreement is demonstrated between this model and the observed behavior of the precipitate feature.

[a]Electronic mail: pjck@isise.rl.ac.uk
[b]Present address: ISIS, Rutherford Appleton Laboratory, Chilton, Didcot, Oxfordshire OX110QX, United Kingdom.

II. DESCRIPTION OF THE SAMPLE

The sample studied consisted of an (001) silicon wafer that had oxidation-induced stacking faults deliberately introduced into its polished top surface and copper deliberately diffused in to form copper silicide precipitates. The partial dislocations associated with the faults acted as nucleation sites for the precipitate particles.

The stacking faults were produced by damaging the wafer surface and then subjecting the wafer to oxidation treatment, as described in Ref. 6. The faults were lying on the four {111} planes of the crystal and were ''*D*''-shaped. They were on average about 15–20 μm long at their intersection with the sample surface, and ran down into the crystal to depths of a few microns where each was bounded by a partial dislocation. The oxide layer was removed from the wafer surface using a hydrogen fluoride etch.

A piece of copper wire was then gently dragged across the back surface of the wafer, and the wafer annealed to allow the copper to diffuse throughout its thickness. The wafer was then allowed to cool to room temperature in a nitrogen atmosphere; the cooling caused the dissolved copper to become supersaturated and precipitation occurred to form copper silicide particles. These particles are known to form either singly or, more likely, as colonies bounded by an edge-type dislocation loop. Colonies, 2–15 μm in length and consisting of many small particles each $\ll 1$ μm in diameter, are known to be produced by this process and form lying parallel to {110} or sometimes {111} planes, which intersect the sample surface plane along [110] or [$\bar{1}$10] directions.[8,9] Colonies are preferentially nucleated at the partial dislocations bounding the stacking faults owing to the tensile strain of the lattice produced by the fault plane. Single precipitate particles up to 0.5 μm in diameter are also known to form near the sample surface.

III. EXPERIMENTAL DETAILS

3 MeV protons, which have a range of 90 μm in silicon, were used for the present work. For CSTIM analysis, the sample must be thin enough to allow the incident MeV ions to be transmitted. The sample was thinned from its rear, unpolished surface to a thickness of 30 μm using wet and dry paper and then diamond lapping compound, which removed large scratches from the thinned surface. It was fixed to a stage allowing rotation about a single (vertical) axis in the sample plane and mounted in the chamber of the Oxford nuclear microprobe.[10] This stage allowed the sample to be tilted through a large angular range for the location of many different planar channeling directions. The proton beam spot was focused to a size of the order of 200 nm and the beam divergence into the channeling planes was 0.03° or less. A semiconductor charged-particle detector with an acceptance half-angle of 0.4° was mounted behind the sample on the beam axis to measure the energy of the transmitted protons. Channeling directions were located by maximizing the fraction of protons transmitted with a higher than normal energy. Images of the sample comprised of 256×256 pixels were produced by recording a transmitted proton energy spectrum as the incident beam was scanned over a region of the sample. The transmitted energy spectrum was divided up into energy windows. The separate images produced from each window were then used to produce a single image showing the mean transmitted proton energy loss at each pixel within the scanned region. A full description of the experimental arrangement and the method of image production can be found in Ref. 2. The images shown here have all been printed in grey scale, with darker greys representing higher mean energy loss. They have been processed with histogram equalization, which assigns equal numbers of pixels to each grey level and increases the contrast in the displayed image; the images have also been smoothed to reduce the effects of noise due to counting statistics.

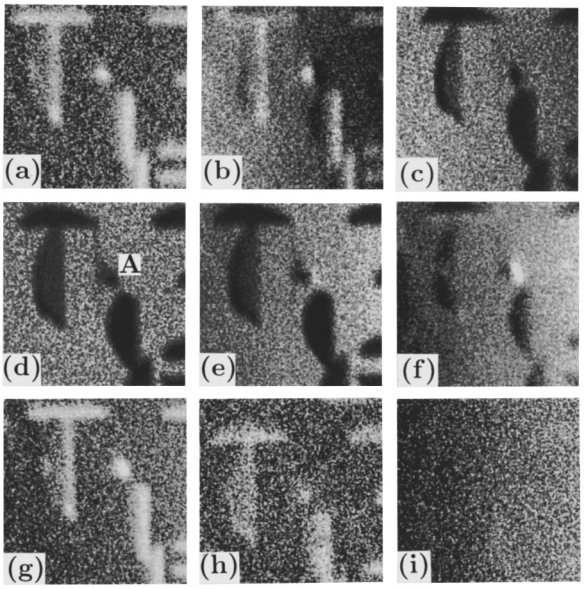

FIG. 1. 35 μm wide CSTIM mean energy loss images recorded with the beam incident at different tilt angles to the (111) channeling planes. Images have been smoothed and printed with histogram equalization. Darker greys represent higher energy loss. Beam angle θ to the (111) channeling planes is (a) −0.17°, (b) −0.11°, (c) −0.06°, (d) 0.0°, (e) +0.06°, (f) +0.11°, (g) +0.17°, (h) +0.31°, and (g) +0.86°. In (d), the precipitate feature is labeled A. The sample [110] and [$\bar{1}$10] directions run, respectively, from left to right and from bottom to top of these images and in the images of Figs. 2–4.

IV. CHANNELING RESULTS

Shown in Fig. 1 is a set of nine 35 μm wide CSTIM mean energy loss images of a portion of the sample. Each image was recorded with the incident beam at a slightly different angle to the (111) channeling planes, which have a channeling critical angle of $\psi_c = 0.1°$ for 3 MeV protons. This channeling direction was reached by mounting the sample with the [110] and [$\bar{1}$10] directions running approximately horizontally and vertically and with the beam normal to the sample surface, and then tilting the sample through 35° about the vertical axis running approximately parallel to the sample [110] direction. The beam was then close to, but not channeled in, the [112] crystal axis. Figure 1(d) was taken with the beam at (111) planar channeling alignment. Two stacking faults lying on (111) planes can be seen (backwards-facing ''*D*'' shapes) together with a third fault lying on a (111) plane (upwards-facing ''*D*'' shape). The

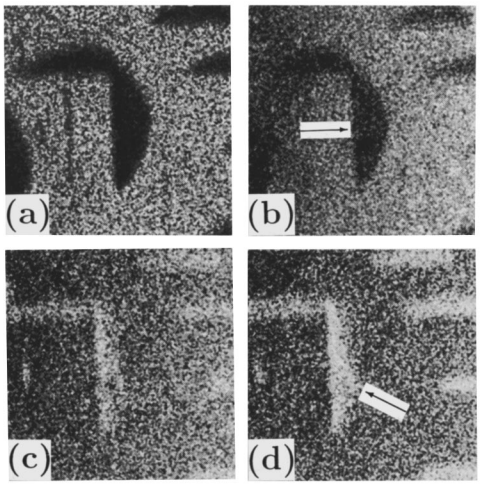

FIG. 2. 35 μm wide CSTIM images of the same sample region as Fig. 1, beam at or close to (111) channeling. Angles from (111) alignment are (a) 0.0°, (b) +0.06°, (c) +0.11°, and (d) +0.17°.

faults are dark grey in this image owing to the dechanneling they produced, locally raising the mean transmitted proton energy loss. Running vertically down from the right-hand end of the (111) fault is a thin, dark line and about half way along this line is a dark, roughly circular feature (labeled A). The dark line is a stacking fault lying on a (111) plane that was end on in this image (see Fig. 2) and the dark feature is considered to be a single precipitate particle or a small colony of precipitate particles (its nature will be discussed again in Sec. VI). The contrast exhibited by this precipitate feature, which will be referred to from here on as the precipitate, is the main subject of this paper.

The image of Fig. 1(a) was taken with the beam at a large tilt angle to the channeling planes. No evidence of the stacking faults or the precipitate can be seen, so the contrast in the other images of Fig. 1 is due to channeling variations and not caused by thickness or density variations produced by the precipitate or stacking faults.

As the sample was tilted so that the beam was incident at different angles to the channeling planes, the contrast shown by the stacking faults and the precipitate changed. Consider first the stacking fault contrast. The faults remain dark in images (c) and (e) with the beam at $\theta=\pm 0.06°$ to the channeling direction, i.e., $\theta=\pm 0.6\psi_c$. With the beam aligned very closely to the channeling critical angle of 0.1°, in images (b) and (f) ($\theta\sim\pm\psi_c$) the contrast in the parts of the faults closest to the sample surface has changed to bright. With the beam aligned beyond the channeling critical angle in images (a), (g), and (h), $\theta>\pm\psi_c$, the whole of each stacking fault appears bright, with the part closest to the sample surface showing strongest contrast. Bright contrast means that the region of the sample was transmitting the protons with a lower mean energy loss than the surrounding crystal. This change in contrast of the stacking faults with tilt angle has been explained previously.[7] With the beam close to channeling alignment, the primary effect of the faults was to cause dechanneling, so they appear dark in CSTIM images. As the beam was tilted to angles just greater than the channeling critical angle, the translation of the lattice at the stacking fault caused some protons traveling on blocked trajectories to be converted to those with well-channeled trajectories. This means that the stacking fault region produced a lower mean energy loss than the surrounding good crystal, and the fault appears bright. This effect occurs most strongly closest to the sample surface, so that the near-surface parts of the stacking faults show the strongest bright contrast.

As well as these primary contrast features exhibited by the stacking faults in Fig. 1, anomalous contrast is also shown by some of the faults. In particular, the upper of the two (111) faults shows strong dark contrast on its curved edge in Figs. 1(c)–1(e), and its deepest part (at the center of its curved edge) is showing strong bright contrast in Figs. 1(a) and 1(g). Such features were shown by other faults in this sample, but were not shown by faults in samples with no copper precipitates. As discussed in Sec. V below, these effects are believed to be due to precipitates associated with the partial dislocations surrounding the faults.

Consider now the contrast shown by the precipitate, labeled A in Fig. 1(d). In Fig. 1(e), taken at a positive tilt angle that was smaller than the channeling critical angle, the very right-hand part of the precipitate begins to show bright contrast. In this image, none of the stacking faults show bright contrast. At a tilt angle of $\theta\sim\psi_c$, in image (f), the precipitate has become half bright and half dark. The interface between bright and dark contrast across the precipitate runs approximately parallel to the channeling planes. In image (g), taken at a larger positive tilt angle of $\theta=1.7\psi_c$, the precipitate exhibits only bright contrast, which it retains out to a tilt angle of $\theta=3\psi_c$, in image (h). For a negative tilt angle the precipitate again shows bright–dark contrast with the beam tilted by $\theta\sim-\psi_c$ away, in image (b), but in this case it is bright on its left side and dark on the right. A larger negative tilt of $\theta=-1.7\psi_c$ again caused the precipitate to go fully bright, image (a). It is assumed that the mechanism for the precipitate's contrast must differ from that of the stacking faults owing to the reversal in bright–dark contrast between the images of Fig. 1(b) and (f), which the stacking faults do not show, and also because the precipitate shows a change of contrast at a much smaller positive and negative tilt angle of $\theta=0.6\psi_c$ than do the stacking faults.

Figure 2 shows CSTIM images of the same region of the sample, but taken with the beam at or close to the (111) channeling alignment. The stacking faults on (111) planes in Fig. 1(d) are now end on and can be seen as vertical, dark lines. The vertical, dark line seen in Fig. 1(d) is now revealed as a fault lying on a (111) plane. As the beam was tilted from the channeling direction, the stacking faults become bright. The effects of the precipitate can only be faintly seen, as a darkening of the stacking fault in Fig. 2(b) (arrowed) and as an extension of the bright part of the fault in Fig. 2(d) (arrowed).

In Fig. 3, images of this same region taken with the beam near the sample normal direction at or close to channeling in the (110) planes are shown. Now the stacking faults on (111) and (111) planes visible in Figs. 2 and 3 can all be seen. However, the (111) fault cannot be seen as it was not affecting the (110) channeling planes.[6] The precipitate is visible as a dark extension of the stacking fault in Fig. 3(c), as

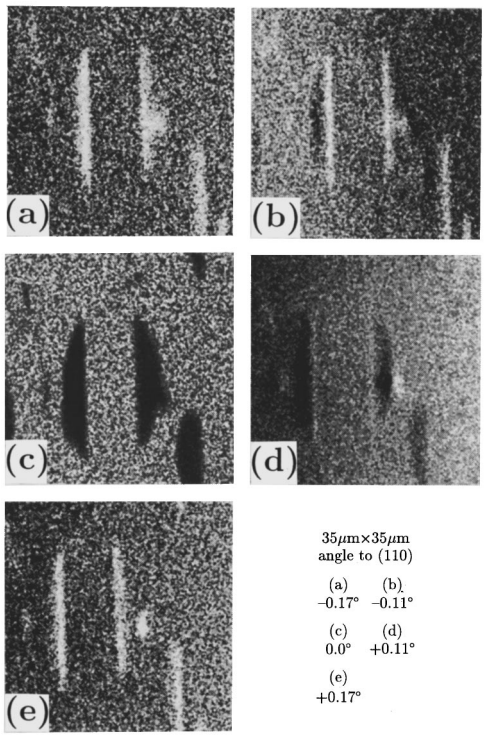

FIG. 3. 35 μm wide CSTIM images of the same sample region as Fig. 1, beam at or close to (110) channeling. Angles to (110) alignment are (a) $-0.17°$, (b) $-0.11°$, (c) 0.0°, (d) $+0.11°$, and (e) $+0.17°$.

a bright region in Figs. 3(a) and 3(e), and as bright–dark regions of opposite contrast in Figs. 3(b) and 3(d).

Finally, Fig. 4 shows CSTIM images taken with the beam at or close to alignment with the orthogonal (110) planes. The stacking fault closest to the precipitate is invisible in these images, but the precipitate can be clearly seen near the center of Fig. 4(a). With the beam tilted by an angle of $\theta \sim \psi_c$ away from the (110) alignment [Fig. 4(c)], the precipitate once again shows bright–dark contrast, but now with the lower part dark and the upper part bright. The interface between bright and dark contrast has remained parallel to the channeling planes. The precipitate is fully bright in the image taken at a tilt angle of $\theta > \psi_c$ [Fig. 4(d)].

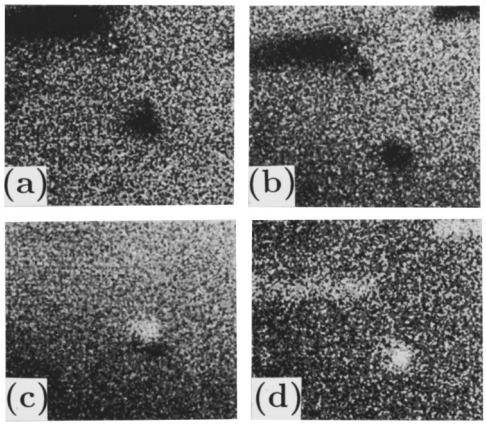

FIG. 4. 30×26 μm wide CSTIM images of the same sample region as Fig. 1, beam at or close to (110) channeling. Angles to (110) alignment are (a) 0.0°, (b) $+0.06°$, (c) $+0.11°$, and (d) $+0.17°$.

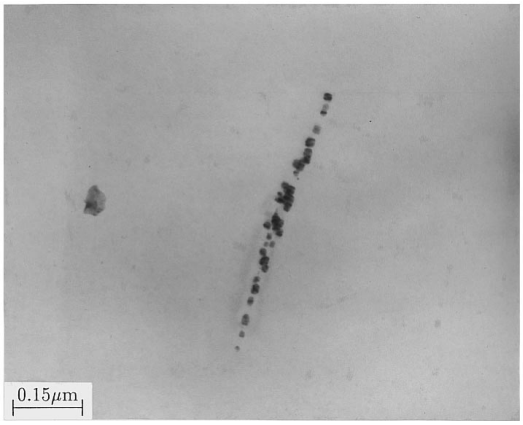

FIG. 5. TEM micrograph of a small precipitate colony.

V. TRANSMISSION ELECTRON MICROSCOPY EXAMINATION

The sample was subsequently thinned from the back surface and examined in plan view by transmission electron microscopy (TEM). Isolated precipitates were not found but precipitate colonies were identified. The majority of the colonies were associated with the bounding partial dislocations of stacking faults. (Approximately 50% of the stacking faults had associated colonies; these colonies may be responsible for the anomalous CSTIM contrast in some stacking fault images referred to earlier.) However, precipitate colonies not associated with partial dislocations also occurred, with a wide range of diameters up to a few microns. One of the smaller colonies of this kind, about 0.4 μm in length, is shown (in an edge-on view) in Fig. 5. This micrograph was taken with the sample tilted away from strongly diffracting conditions in order to reveal the individual precipitates clearly. Images taken in strongly diffracting conditions show the existence of strain around this colony, as well as around other colonies.

VI. MODEL OF THE PRECIPITATE CONTRAST

The precipitate contrast described in Sec. IV is believed to have been caused by the presence of a small copper silicide precipitate colony similar to those seen during TEM examination. The contrast displayed by this region of the sample is unlike that shown by the neighboring stacking faults, so that a different explanation of the contrast is necessary. It is considered that the contrast within the precipitate region is not due to the individual particles themselves being imaged, as they would have been too small to be resolved with a beam spot size of the order of 200 nm. Rather, it will be shown below that the contrast is consistent with the effects on channeling of elastic strain producing rotated lattice planes within the region.

From the CSTIM images shown in Figs. 1–4, the net effect of the precipitate was (i) to cause dechanneling when the incident beam was close to channeling alignment, so that the precipitate appeared dark, (ii) to enhance channeling above that of the surrounding perfect (virgin) crystal for a positive or negative tilt angle of $\theta > \psi_c$, so that the precipitate

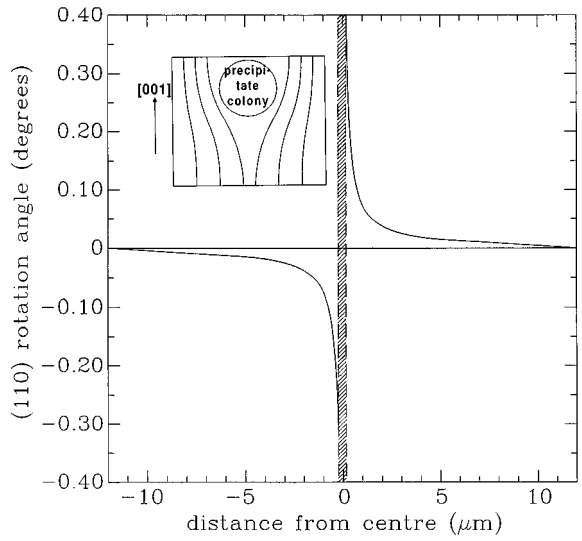

FIG. 6. Plane rotation assumed for the strain field around the precipitate particles. The shaded region in the center is where very large rotations would have occurred, and no simulations were done for this region. A sketch of the planes around a precipitate is given in the inset.

appeared bright, and (iii) to show a combination of these effects with the beam tilted to $\theta \sim \pm \psi_c$ so that the precipitate appeared partly bright and partly dark. The precipitate showed bright–dark contrast with the beam to one side of a channeling direction and dark–bright contrast with the beam to the other side.

Previous work showing spatially resolved images of misfit dislocations in $Si_{1-x}Ge_x$/Si crystals[2–4] revealed that these defects could locally enhance channeling (producing bright image contrast) for incident beams just away from exact channeling alignment. This effect was interpreted as being caused by lattice plane rotations in the $Si_{1-x}Ge_x$ layer produced by the dislocation strain field. When the incident beam was aligned with the rotated planes (and misaligned with the substrate channeling direction) channeling occurred more readily than in the surrounding perfect crystal. For small plane rotations, this was found to occur for beam incident angles of less than the channeling critical angle away from alignment.

The presence of precipitate particles in a matrix produces a local strain field leading to lattice plane rotation. Unlike the case of misfit dislocations described above, this rotation would be approximately spherically symmetrical around each colony of particles, with lattice planes on opposite sides being rotated in opposite directions. We assume here that the strain field at distances from a linear colony that are large compared with the colony size will also be approximately spherical, with lattice planes being rotated outwards from the colony as for a spherical precipitate. A sketch of this situation is given in the inset of Fig. 6. The evidence for such local plane rotation in the precipitate region of this sample comes from several features of the images given in Figs. 1–4. First, the reversal of the precipitate contrast from bright–dark to dark–bright with the beam on opposite sides of the channeling direction is consistent with lattice planes on opposite sides of the feature being rotated in opposite senses. That the boundary between bright and dark contrast remained parallel to the channeling plane normal direction suggests that the strain field was spherically symmetrical. The edges of the precipitate showed bright contrast first (with the boundary between the bright and dark regions moving across the feature with increasing tilt angle). This is consistent with a strain field, as regions where the plane rotations were small at the edge of the field would enhance channeling at small tilt angles. It can be determined from the sense of tilt of the beam with respect to the sample that for the bright–dark contrast to occur on the side of the precipitate that it did in the images of Figs. 1(b), 1(e), and 1(f), the lattice planes would have been rotated outwards from the center of the precipitate region. This is consistent with precipitates being in compression and being located near to the sample surface. Evidence for the precipitate being near to the sample surface also comes from the fact that its position with respect to the (111) and (110) stacking fault edges in Figs. 1–4 changes little with sample tilt angle.

A. Simulation of dechanneling from rotated lattice planes

In order to verify that these observed features may be considered to be due to plane rotations in the precipitate region of the sample, we use here Monte Carlo computer simulations of the passage of 3 MeV protons through a crystal with lattice planes near its surface rotated. For simplicity, we assume a spherical precipitate particle, and consider the plane rotation around the precipitate to be symmetrical about the precipitate center and to decrease as the reciprocal of the distance from the center of the precipitate region.

Shown in Fig. 6 is a plot of the lattice plane rotation that was assumed. The plane rotation is large close to the precipitate and then falls off rapidly. The region up to ± 200 nm away from the center of the rotated planes is shown in hatched lines. In this region the plane rotation would be very large compared with the channeling critical angle according to our model. No Monte Carlo channeling simulations were performed for such large rotation angles and no further consideration is given to this region. Rotation of the form shown in Fig. 6 was assumed to occur in a circularly symmetrical manner about the precipitate region. The size of the plane rotation was empirically chosen so that the lateral extent over which channeling contrast occurred in the simulations was similar to that observed experimentally.

A rigorous simulation of the effects on channeling of the rotated planes around the precipitate would take into account the depth variation of the plane rotation angle. Simulation programs are not presently available to do this, so the simplifying assumption is made here that the lattice planes throughout the whole depth of a thin surface layer were rotated as shown in Fig. 6. The approach used here can only, therefore, be expected to serve as a guide to the general dechanneling behavior of precipitate particles with beam angle to the channeling planes. A bilayer structure was used in these simulations, consisting of a 1 μm thick silicon epilayer on a 19 μm thick silicon substrate. An adapted version of the computer program FLUX3 (Refs. 11, 12, and 13) was used for these Monte Carlo simulations, in which the regions

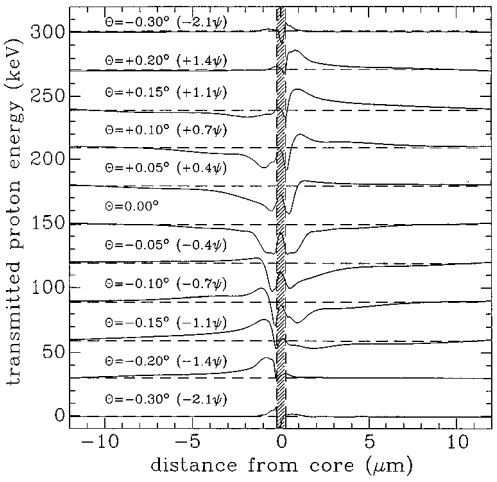

FIG. 7. Variation of the average transmitted proton energy across a region with planes rotated as shown in Fig. 6. Curves produced from Monte Carlo simulations made by the FLUX3 program, for a range of positive and negative tilt angles from the substrate [001] axis, in the (110) planes. The curves assume a point beam spot. The curves are plotted relative to the transmitted proton energy in the surrounding perfect crystal at each sample tilt angle, which is given a value of 0 keV in each case and shown as the horizontally running dashed lines. Each curve is offset by an additional 30 keV for clarity. No simulations were performed for the hatched region near the center of the plots.

on both sides of the bilayer boundary were assumed to be perfect silicon crystal. The top layer was given a rotation angle δ, with respect to the bulk about the [110] axis, lying in the boundary plane. For all the simulated results the bilayer sample was tilted away from the substrate [001] axis, in the (110) planes, such that channeling in the (110) planes only was altered.

Features of the average transmitted proton energy vs θ, the beam angle to channeling alignment, and δ, the plane rotation angle, are related to the critical angle for the transition from axial to planar channeling, $\psi_c = 0.14°$, for 3 MeV protons in this case. For each combination of rotation angle and the tilt angle θ of the sample as a whole with respect to the beam, the average proton energy after transmission through the bilayer was determined. No account was taken of the angular distribution of the transmitted protons leaving the crystal. The statistical noise level on the simulated results was 1 keV for each value of the simulated average proton energy at each tilt angle and rotation angle. These curves showing the simulated average transmitted proton energy as a function of tilt angle for various plane rotation angles are given in Ref. 4.

B. Simulated results for symmetric lattice plane rotation

Figure 7 shows the predicted variation of the average transmitted proton energy across a region of the bilayer crystal with the lattice planes of the top layer rotated in a symmetric manner for a range of positive and negative tilt angles of the beam from the substrate [001] axis in the (110) planes. Figure 7 was constructed using the Monte Carlo simulated curves as a function of θ and δ, assuming a plane rotation as shown in Fig. 6. These curves assume a 3 MeV proton beam focused to an insignificantly small point on the silicon surface. The region up to ± 200 nm away from the center is shown in hatched lines and no simulations were performed to model the behavior in this region.

In [001] alignment (i.e., $\theta = 0.0°$) the variation of the transmitted proton energy is symmetrical about the center of the region with rotated planes because the (110) planes are rotated by an equal, but opposite, amount on either side. There is a region of uniformly low average transmitted proton energy within a distance of 1 μm from the center owing to the large amount of dechanneling by the proton beam passing through the highly rotated (110) planes. The average transmitted proton energy gradually increases away from the center towards that of the surrounding perfect crystal owing to a reduction of the dechanneled beam fraction caused by a decrease in rotation of the (110) planes.

When the sample is tilted away from the [001] axis in the (110) planes, the spatial variation of the transmitted proton energy becomes asymmetric about the center. A negative tilt angle of $\theta < -1.5\psi_c$ gives, respectively, a higher and a lower transmitted proton energy on the left and right sides of the center than from the surrounding perfect crystal. Where the rotated planes produce an average transmitted proton energy higher than for the surrounding perfect crystal, the plane rotation is enhancing the channeling effect on those protons that would otherwise dechannel in a perfect crystal.[4] This occurs because the rotated (110) planes on the left side of the center become better aligned with the incident proton beam at a positive tilt angle. The (110) planes on the right side of the center are more misaligned with the incident proton beam for a positive tilt angle, so there is a progressively larger region of lower transmitted proton energy. For a tilt angle of $\theta < -1.7\psi_c$ the only resolvable proton energy variation relative to the surrounding perfect crystal is a narrow region of increased proton energy to the left of the center.

A positive tilt angle away from the [001] axis in the (110) planes gives a similar effect but with the regions of higher and lower transmitted energy reversed. The transmitted proton energy across planes rotated in a symmetric manner shown in Fig. 7 thus varies in a symmetric manner about the center with tilt angle.

1. Maximum contrast across the rotated lattice planes

In this work a positive contrast is defined as where the average transmitted proton energy is lower at the rotated planes, and a negative contrast is where the average proton energy is higher at the rotated planes than in the surrounding perfect crystal.

Figure 8(a) shows the maximum positive and negative energy contrast observed at any position across the rotated planes as a function of sample tilt angle, based on Fig. 7. The positive contrast has a maximum value at $\theta = 0.0°$, at which tilt angle the negative contrast is zero since there is no region where channeling is enhanced by the plane rotation. The negative contrast is a maximum at $\theta \sim \pm 1.2\psi_c$. At positive and negative tilt angles of $\theta > 2.2\psi_c$, neither the maximum negative nor positive contrast is large enough to be resolved from the noise level, so the entire region of symmetric plane rotation becomes ''invisible.''

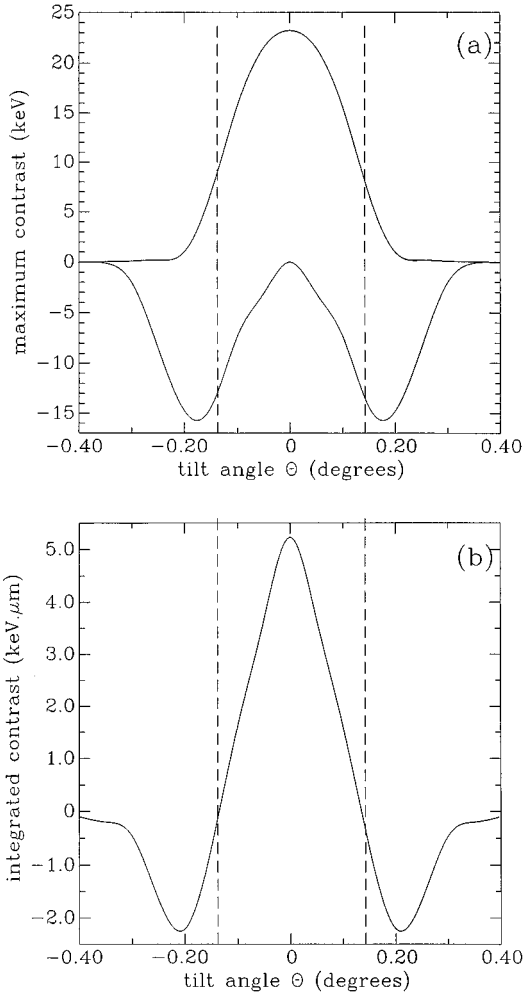

FIG. 8. (a) Maximum positive and negative contrast at any position across the region of rotated lattice planes as a function of sample tilt angle from the substrate [001] axis, in the (110) planes. (b) Integrated contrast from the region of rotated lattice planes as a function of sample tilt angle from the substrate [001] axis, in the (110) planes. For (a) and (b), the curves are symmetric about $\theta=0.0°$, i.e., a negative tilt angle gives identical curves.

2. Integrated contrast from the rotated lattice planes

The definition of ''integrated contrast'' is used to further characterize the effect on protons channeling through the rotated lattice planes around the precipitate. The integrated contrast represents the total difference in transmitted proton energy compared with the surrounding perfect crystal over a region just larger than the maximum extent of the observable contrast away from the core (a distance of ± 10 μm in this case), i.e., this is where the energy contrast is the same size as the noise level. A positive integrated contrast means that the net transmitted proton energy at the rotated planes is lower than in the perfect crystal, and a negative integrated contrast means the opposite.

Figure 8(b) shows the variation of the integrated contrast with sample tilt angle from the [001] axis in the (110) planes for the rotated lattice planes. It was constructed by integrating the curves in Fig. 7 with respect to the transmitted proton energy from a perfect crystal at each tilt angle. For a positive or negative tilt angle of $\theta<\psi_c$ the integrated contrast is positive, i.e., there is a net reduction in transmitted proton energy

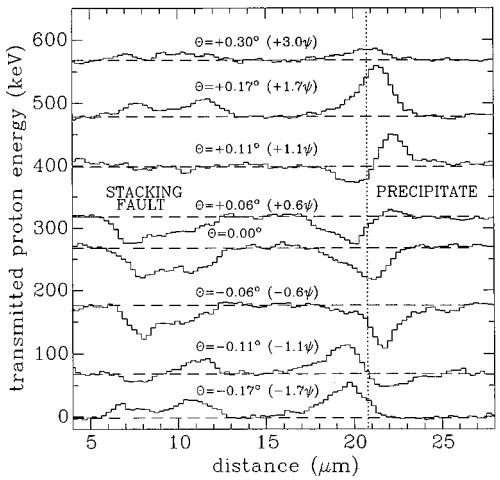

FIG. 9. Line scans extracted from the images of Figs. 1(a)–1(h). They show one of the (111) stacking faults seen in Fig. 1, the right-hand edge of which was used to align the line scans laterally, and the precipitate. The vertical, dotted line passes through the center of the precipitate and is a guide to the eye to show the shift in the feature. Each line scan is labeled with the beam angle to (111) channeling. The line scans are plotted relative to the transmitted proton energy for the crystal region surrounding the fault and precipitate at the given angle, and this level is given a value of 0 keV and shown by the horizontal dashed lines. Each line scan is offset from the one below for clarity.

at the region of plane rotation. For a positive or negative tilt angle of $\psi_c<\theta<2.2\psi_c$ the integrated contrast is negative, i.e., there is a net increase in transmitted proton energy, which is smaller than the maximum positive contrast. Where the integrated contrast passes through zero at a tilt angle of $\theta\sim\pm\psi_c$, the average transmitted proton energy measured at, and away from, the region of rotated planes is the same. At this tilt angle, the rotated planes cause an equal amount of channeling and dechanneling compared with the perfect crystal.

VII. COMPARISON OF CONTRAST FROM THE PRECIPITATE REGION WITH THAT PREDICTED FROM THE MODEL

Figure 9 shows horizontal line scans extracted from the CSTIM images in Fig. 1 from across the middle of the precipitate. They show the stacking fault on the left-hand side and precipitate on the right-hand side. Each line scan was produced from the average of 7 rows of pixels (equivalent to averaging over a vertical distance of 1 μm on the images). The line scans were smoothed in groups of ± 2 pixels (i.e., ± 0.3 μm) to reduce the effects of statistical noise. They have been horizontally aligned with each other by ensuring that the right-hand side of the stacking fault occurs at the same point in each; this was necessary because the slight noneucentricity of the sample tilt stage meant that the sample underwent small translations as it was tilted. These line scans can now be compared with the simulated line scans shown in Fig. 7 that assumed symmetric plane rotation. Only a qualitative comparison can be made since the simulated results (i) assumed a simple bilayer structure to model the plane rotation, (ii) assumed that the plane rotation occurred abruptly at a depth of 1 μm beneath the surface, (iii) show the variation

of the average energy of all the transmitted protons whereas the experimental results show the variation in average energy for protons transmitted within a half-angle of 0.4° about the beam axis in order to increase the energy contrast, and (iv) use different channeling planes.

First consider a tilt angle of $\theta=0.0°$. In the simulated results, there is a large region of low transmitted energy that is symmetric about the center whereas in the measured results there is similarly a region of low transmitted energy that is, however, slightly asymmetric. For a positive tilt angle of $\theta<\psi_c$, there is a region to the right of the center where there is high transmitted energy. This increases in size in both the measured and simulated results with increasing positive tilt angle. Also, there is a region to the left of the center where there is low transmitted energy that decreases in size with increasing positive tilt angle. For a positive tilt angle of $\theta>1.2\psi_c$, there is scarcely any region of low transmitted energy, and the peak of high transmitted energy lies about 0.7 μm to the right of the center.

For a negative tilt angle, the measured and simulated results exhibit similar changes in contrast in which there is a region of high transmitted energy now to the left of the center. For $\theta\sim\pm1.5\psi_c$, the displacement between the spatial positions of the maxima of transmitted energy is a distance of ~1.5 μm in both the measured and simulated results. The measured channeling results from across the precipitate thus display all the general characteristics associated with a region of symmetric lattice plane rotation as shown in Fig. 7.

Figure 10(a) shows the measured maximum positive and negative energy contrast from across any position of the measured line scans in Fig. 9, and can be compared with the simulated case in Fig. 8(a). Similarly, Fig. 10(b) shows the measured integrated contrast from the line scans in Fig. 9 that can be compared with that from the simulated line scans in Fig. 8(b). The maximum positive contrast peaks at a tilt angle of $\theta=0.0°$ in the simulated results and slightly away from this in the measured results. In both cases the positive contrast decreases to zero at $\theta\sim\pm1.4\psi_c$. The maximum negative contrast is zero at a tilt angle of $\theta=0.0°$, reaches a maximum at $\theta\sim\pm1.4\psi_c$, and decreases again to zero at $\theta\sim\pm2.5\psi_c$. The integrated contrast is a maximum in both cases at $\theta=0.0°$, passes through zero at $\theta\sim\pm\psi_c$, reaches a minimum at $\theta\sim\pm1.5\psi_c$, and again increases to zero at $\theta\sim\pm3\psi_c$.

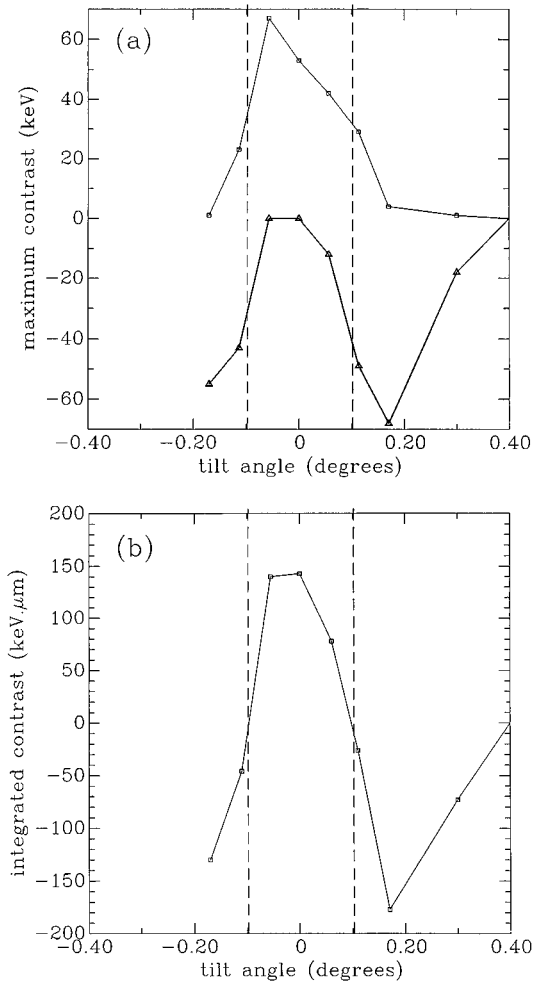

FIG. 10. (a) Maximum positive and negative contrast shown by the precipitate with tilt angle from the (111) channeling planes, measured from the line scans of Fig. 9. (b) Integrated contrast measured from the precipitate with tilt angle from the (111) channeling planes, also from Fig. 9.

VIII. DISCUSSION

In transmission electron microscopy (TEM),[14] the contrast produced by a precipitate may be attributed to two sources: the effects of the precipitate on the host crystal (''matrix contrast'') and the effects of the precipitate itself (''precipitate contrast''). The former effect is due to the elastic strain produced in the crystal by the presence of the particle.

It has been shown above that, for ion channeling, the contrast produced by precipitates that cannot themselves be imaged owing to their small size can be well explained by consideration of the strain field they produce, i.e., it can be described as matrix contrast. Work is at present underway in Oxford to produce a focused beam spot size of the order of 20 nm, and it is not, therefore, unreasonable to expect the imaging of the individual precipitates to be possible in the near future. In that case, effects due to the interaction of channeled protons with the precipitates themselves would be expected. In particular, a proton passing through a precipitate would encounter a new crystal surface when it reentered the host crystal.[1] This would be similar to a proton passing through a stacking fault, so that contrast similar to that produced by faults may be expected in addition to the strain field contrast. It is possible that some of the bright contrast produced by the precipitate in the images shown here with the beam beyond the channeling critical angle away from alignment was produced by a mechanism similar to that outlined for the bright stacking fault contrast. The scattering of channeled ions by an incoherent precipitate and variations in ion energy loss due to precipitates of different density to the host crystal, would also need to be considered in the interpretation of CSTIM images of individual precipitate particles.

IX. CONCLUSIONS

We have shown that transmission ion channeling images of the strain field around a colony of precipitate particles in

silicon can be generated using a focused MeV proton beam from a nuclear microprobe. Features of the precipitate contrast observed as a function of beam tilt angle away from channeling alignment are in good qualitative agreement with a model of spherically symmetric plane rotation of the crystal lattice. This plane rotation simulated in this model is similar to that which may be expected to occur around an edge dislocation on going from the dislocation along a line parallel to the Burgers vector. This work is, therefore, important in providing a future reference basis for interpreting ion channeling images of these defects.

Future work will investigate further the possible contrast effects of the precipitate particle itself which have been suggested above, and will explore the channeling contrast produced by 90° dislocations.

ACKNOWLEDGMENTS

P.J.C.K. and P.R.W. would, respectively, like to thank the Royal Commission for the Exhibition of 1851 and the Royal Society, for Fellowships. Thanks are due to Dr. R. Falster of Monsanto Electronic Materials Corporation for provision of the stacking fault sample and to A. Amaku, Department of Materials, University of Oxford, for performing the copper diffusion.

[1] L. C. Feldman, J. W. Mayer, and S. T. Picraux, *Materials Analysis By Ion Channeling* (Academic, New York, 1982).
[2] M. B. H. Breese, P. J. C. King, J. Whitehurst, G. R. Booker, G. W. Grime, F. Watt, L. T. Romano, and E. H. C. Parker, J. Appl. Phys. **73**, 2640 (1993).
[3] P. J. C. King, M. B. H. Breese, P. R. Wilshaw, G. R. Booker, G. W. Grime, F. Watt, and M. J. Goringe, in *Microscopy of Semiconducting Materials*, edited by A. G. Cullis, A. E. Staton-Bevan, and J. L. Hutchinson (Institute of Physics, 1993), Ser. 134, p. 153.
[4] M. B. H. Breese, P. J. C. King, P. J. M. Smulders, and G. W. Grime, Phys. Rev. B **51**, 2742 (1995).
[5] P. J. C. King, M. B. H. Breese, P. J. M. Smulders, A. J. Wilkinson, G. R. Booker, E. H. C. Parker, and G. W. Grime, Appl. Phys. Lett. **67**, 3566 (1995).
[6] P. J. C. King, M. B. H. Breese, P. R. Wilshaw, and G. W. Grime, Phys. Rev. B **51**, 2732 (1995).
[7] P. J. C. King, M. B. H. Breese, P. R. Wilshaw, and G. W. Grime, Phys. Rev. Lett. **74**, 411 (1995).
[8] M. de Coteau, P. R. Wilshaw, and R. Falster, in *Proceedings of 7th Oxford Conference on the Microscopy of Semiconducting Materials*, edited by A. G. Cullis and N. J. Long (Institute of Physics, 1991), Ser. 117, p. 231.
[9] M. de Coteau. Ph.D. thesis, University of Oxford, 1993.
[10] G. W. Grime, M. Dawson, M. Marsh, I. C. McArthur, and F. Watt, Nucl. Instrum. Methods B **54**, 52 (1991).
[11] P. J. M. Smulders and D. O. Boerma, Nucl. Instrum. Methods B **29**, 471 (1987).
[12] P. J. Smulders , D. O. Berma, and M. Shaanan, Nucl. Instrum. Methods B **45**, 450 (1990).
[13] A. Dygo, W. N. Lennard, I. V. Mitchell, and P. J. M. Smulders, Nucl. Instrum. Methods B **90**, 161 (1994).
[14] P. Hirsch, A. Howie, R. Nicholson, D. W. Pashley, and M. J. Whelan, *Electron Microscopy of Thin Crystals* (Krieger, Florida, 1977).